Icarus 333 (2019) 481–495

Contents lists available at ScienceDirect

Icarus

journal homepage: www.elsevier.com/locate/icarus

Global seasonal variations of the near-surface relative humidity levels on present-day Mars

Bernadett Pál[a,*], Ákos Kereszturi[a], François Forget[b], Michael D. Smith[c]

[a] Research Centre for Astronomy and Earth Sciences, Konkoly Thege Miklos Astronomical Institute, Budapest, Hungary
[b] LMD, Institut Pierre Simon Laplace Université Paris 6, BP 99, 4 place Jussieu, Paris 75005, France
[c] NASA Goddard Space Flight Center, Greenbelt, MD 20771, United States

ARTICLE INFO

Keywords:
Mars
Liquid water
Relative humidity
Habitability
Atmospheric modelling

ABSTRACT

We investigate the global seasonal variations of near-surface relative humidity and relevant attributes, like temperature and water vapor volume mixing ratio on Mars using calculations from modelled and measurement data. We focus on 2 AM local time snapshots to eliminate daily effects related to differences in insolation, and to be able to compare calculations based on modelling data from the Laboratoire de Météorologie Dynamique Mars General Circulation Model with the observations of Mars Global Surveyor Thermal Emission Spectrometer. We study the seasonal effects by examining four specific dates in the Martian year, the northern spring equinox, summer solstice, autumn equinox, and winter solstice. We identify three specific zones, where the near-surface relative humidity levels are systematically higher than in their vicinity regardless of season. We find that these areas coincide with low thermal inertia features, which control surface temperatures on the planet, and are most likely covered with unconsolidated fine dust with grain sizes smaller than ~ 40 μm. By comparing the data of relative humidity, temperature and water vapor volume mixing ratio at three different heights (near-surface, ~ 4 m and ~ 23 m above the surface), we demonstrate that the thermal inertia could play an important role in determining near-surface humidity levels. We also notice that during the night the water vapor levels drop at ~ 4 m above the surface. This, together with the temperature and thermal inertia values, shows that water vapor likely condenses in the near-surface atmosphere and on the ground during the night at the three aforementioned regions. This condensation may be in the form of brines, wettening of the fine grains by adsorption or deliquescence. This study specifies areas of interest on the surface of present day Mars for the proposed condensation, which may be examined by in-situ measurements in the future.

1. Introduction

The occurrence of liquid water is one of the most important components we are seeking during the search for habitable locations outside planet Earth. Mars has been of key importance in the search for extraterrestrial life for decades now (Gargaud et al., 2011). During its geological history there were periods when the planet likely had lakes (Cabrol and Grin, 1999; Ehlmann et al., 2016; Fassett and Head, 2008), rivers or maybe even larger bodies of liquid water (Tokano, 2005). A recent discovery of organic molecules found at Gale crater provided further arguments that Gale crater was potentially habitable about 3.5 billion years ago (Kate, 2018). However, liquid water cannot be sustained in large volumes at the surface of present day Mars mainly due to the thin atmosphere, low temperature and general dryness. Based on recent results, liquid water might emerge on a microscopic scale on the surface of hygroscopic minerals (Nikolakakos and Whiteway, 2018), when the atmosphere shows elevated humidity and the temperature is suitable for various hygroscopic salts (Pál and Kereszturi, 2017). The Rover Environmental Monitoring Station (REMS) of the Curiosity rover showed through meteorological observations, that the necessary atmospheric conditions are met (Martín-Torres et al., 2015), although not certainly everywhere as illustrated in the work of Rivera-Valentín et al. (2018). The existence of liquid water or brines (Zorzano et al., 2009) is indicated in several other observations as well, that might support some movement on the Martian surface in the form of streaks emanating from Dark Dune Spots (Kereszturi and Rivera-Valentin, 2012, 2016) and changing droplet-like features on the leg of the Phoenix lander (Rennó et al., 2009). Recurring Slope Lineae (McEwen et al., 2011; Ojha et al., 2015) are also presumed to be connected to some form of liquid, however Dundas (2018) showed that

* Corresponding author.
E-mail address: pal.bernadett@csfk.mta.hu (B. Pál).

https://doi.org/10.1016/j.icarus.2019.07.007
Received 23 August 2018; Received in revised form 5 July 2019; Accepted 10 July 2019
Available online 12 July 2019
0019-1035/

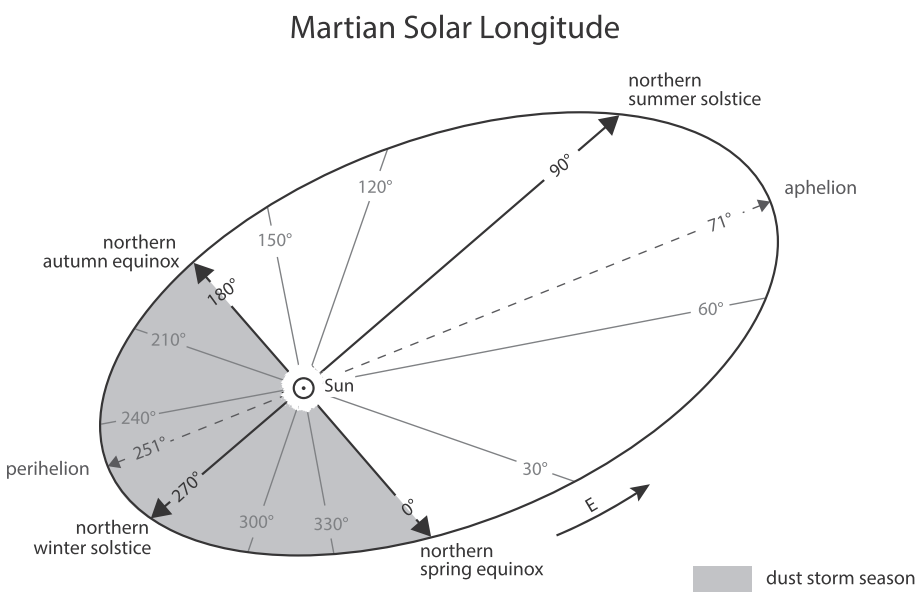

Fig. 1. Martian solar longitude. A Martian year is 668.59 Martian days (sols) long, which is equal to 687 Earth days, because a sol is 24.623 hours long, ~ 40 minutes longer than a day on Earth (Clancy et al., 2000). To mark the time on Mars it is common to use the local time in Martian hours with a sol divided by 24 and the areocentric longitude of the Sun (Ls) as viewed from the centre of Mars. This is equivalent to ecliptic longitude.

these are largely consistent with the dust-avalanche model. The main goal of this study is to explore the global behavior of near-surface relative humidity during different seasons (Fig. 1) and daily cycles at different locations to improve our general understanding where and when liquid water could be sustained. It is also aimed at contributing to future mission planning by showing locations with elevated relative humidity levels and possible related processes, for example, deliquescence.

Saturation and supersaturation have to occur occasionally on Mars to produce the observed surface condensation of water ice and the aphelion cloud belt. Supersaturation has been observed in the Martian atmosphere (Maltagliati et al., 2011a) by SPICAM onboard Mars Express mission. Some former models suggested that supersaturation might be rare on Mars (Richardson et al., 2002) because of instantaneous formation of ice (Montmessin et al., 2004), or predicted it to occur at higher altitudes Moores et al. (2011). The occurrence of nighttime saturation has been suggested earlier (Davies, 1979; Savijärvi, 1995), however previously most works focused on saturation at a substantial elevation above the surface, causing cloud condensation (Gurwell et al., 2000) and fog condensation, especially during the night (Davies, 1979; Moores et al., 2011). Based on microwave temperature and water profiling at low- to mid-latitudes, saturation occurs below 10 km during northern spring/summer (Clancy et al., 1996). The annual migration of saturation height has been confirmed by OMEGA data, showing 5–15 km height during aphelion, while it stretches up to 55 km during perihelion (Maltagliati et al., 2011b). Surface saturation produced condensation might happen at low latitudes because of the very cold nights on Mars (Carrozzo et al., 2009), and at the low thermal inertia regions, where for example CO_2 condensation occurs also as described in Piqueux et al. (2017). The spatial and temporal pattern of saturation migrates by climate changes too, probably it moves toward the equator during the increase of orbital tilt (Forget et al., 2006; Jakosky and Carr, 1985; Madeleine et al., 2009). In the light of the available literature, this is the first time global near-surface relative humidity was analyzed in such detail.

2. Methods

We investigated the global variations of the relative humidity (RH) at the surface by two different approaches. First, we examined model calculations by the Laboratoire de Météorologie Dynamique Mars General Circulation Model (LMDZ GCM), detailed in Forget et al. (1999), including a water cycle as described in Navarro et al. (2014). Second, we looked at the measurements of Mars Global Surveyor Thermal Emission Spectrometer (MGS TES) (Smith, 2006) and calculated RH values from the available temperature (T) (Conrath et al., 2000), pressure (P) and water vapor data (Smith, 2002). A flowchart showing the schematic way of our calculation methods is shown in Appendix B.

Our maps are represented on an equirectangular latitude-longitude grid. Each map is a snapshot of the planet, where the local time does not change with geographical longitude. These are composite maps with the same local time (LT) everywhere, e.g. if it is 2 AM LT at 0° E, it is also 2 AM LT at 120° W. The maps illustrating calculations from GCM modelled data are either near the surface, or at approximately 23 m, always indicated in the titles. In calculating relative humidity values at the surface, we used surface temperature, surface pressure and the water vapor volume mixing ratio (VMR) at 4 m height (the first atmospheric level in GCM), and presumed the water vapor to be well mixed between the surface and the first layer. This way of calculating will be referred to as near-surface in the following.

To get the RH values, the saturation VMR is needed. This can be calculated with the following equation used in the MCD model, which is based on the Tetens formula:

$$Q_{sat} = \frac{100}{P} \times 10^{2.07023 - 0.00320991T - \frac{2484.896}{T} + 3.56654\log(T)} \quad (1)$$

where P is the surface pressure and T is the surface temperature.

After determining the necessary Q_0 value, the RH can be calculated as:

$$RH = \frac{Q_0}{Q_{sat}} \quad (2)$$

2.1. GCM modelling data

Our first approach in determining the global distribution of RH was through modelling. For this, we used the data file created by the LMDZ GCM version 5 (current version), which correspond to Navarro et al. (2014) and Pottier et al. (2017). The file contained simulated data for the whole Martian Year 29. This numbering of Martian years is widely used and follows the calendar proposed by R. Todd Clancy (Clancy et al., 2000), which begins on April 11, 1955 (Ls = 0°). The year 29 is without a global planet-encircling dust storm. The data came in a NetCDF format which we handled with different C and C++ programs of our own and visualized with Panoply.

The VMR calculations are not reliable under ~ 4 m due to the complexity of modelling near-surface interactions. For this reason in our study we used the ~ 4 m VMR data together with surface temperature (ST) and surface pressure (SP) values to estimate near-surface RH by assuming the vapor to be well mixed between the surface and ~ 4 m. Because we compare atmospheric vapor values with TS, the RH numerical values can reach unrealistically high outliers in some locations. Physically the supersaturation never goes very high, because the nighttime atmosphere is much warmer than the surface, and just near it the atmosphere is drier due to the interaction with the surface. In some way we show a "potential supersaturation" assuming that the water vapor at ~ 4 m reflects the value at the surface. While the specific numerical values might not be accurate in all locations, the distribution of elevated relative humidity is reliable, which is why we concentrate on the global scale in this study, and refer to the changing of values only in relative terms.

2.2. TES data

The Mars Global Surveyor (MGS) was launched on November 7, 1996 and was successfully put into orbit around Mars on September 12, 1997. The mission ended on November 2, 2006, when the mission controllers lost contact with the spacecraft. The TES instrument measured and monitored the Martian surface and atmosphere throughout the mission and collected over 206 million infrared spectra of the thermal infrared energy (heat) emitted from Mars (Smith, 2004, 2006). This survey also provided the first detailed look at the surface composition of Mars.

To easily compare GCM results with the TES measurement data, we created a NetCDF format file from the TES data files as well. For the NetCDF format the data is required to be on an equally spaced grid, we modified the TES results by filling the absent measurement points with "−1" values. The resulting NetCDF file has 207 Ls ($\Delta Ls = 5^{\circ}$), 60 latitude ($\Delta lat = 3^{\circ}$) and 48 longitude ($\Delta lon = 7.5^{\circ}$) grid points, and thus 596 160 data points. The data were acquired between July, 1998 and January, 2006 from the 24th Martian year to the 27th. The estimated uncertainty for water vapor abundance is ± 3 precip-microns or 10%, whichever is greater. For the temperature data the uncertainty is approximately ± 2–4 K.

For the RH values, we first needed to determine the VMR. Details of the mixing ratio calculation can be seen in Appendix A. The column mass of water vapor is:

$$m_{H_2O} = 0.001 \times \text{TES}_{H_2O}\ \text{column (kg m}^{-2}) \tag{3}$$

with TES_{H_2O} column measured by TES in precipitable microns. If we assume that water vapor is confined below a pressure level p_{top} (Pa), the mean mass mixing ratio between p_{surf} and p_{top} is:

$$\text{mmr} = \frac{m_{H_2O} \times g}{p_{surf} - p_{top}} \tag{4}$$

with gravity denoted by g (m s^{-2}). The corresponding volume mixing ratio is:

$$Q_0 = \text{mmr} \times \frac{44}{18} \tag{5}$$

with 44 g mol^{-1} and 18 g mol^{-1} being the molar mass of Martian air and water, respectively.

In this estimation, we assumed that water vapor is well mixed, which means that the mixing ratio is constant from the surface (p_{surf}) to a certain height in the atmosphere (p_{top}). The most simple way is to choose p_{top} to be equal to 0. This means that there is no "upper limit ", the water vapor extends through the atmosphere. A more realistic approach would be if we take the pressure level as the value of p_{top} where the water vapor condenses, also known as the **condensation height** (Smith, 2002). Knowing the condensation levels as a function of solar longitude and latitude, and choosing 10 km as the pressure scale height:

$$p_{top} = p_{surf} \times e^{-z_{top}/10\ \text{km}} \tag{6}$$

where z_{top} denotes the condensation height given in kilometers. After calculating Q_0 this way, Eq. (2) can be used to determine the RH directly above the surface.

Reliable water vapor retrievals have only been performed on the TES daytime observations, so in our TES calculations we used TES water vapor data from approximately 2 PM together with approximately 2 AM TES ST and SP data. To estimate the validity of substituting daytime vapor measurements in nighttime calculations, we computed RH for 3 Martian years using nighttime TES ST and SP data, and we took VMR modelled first for 2 AM and then for 2 PM from GCM. For this, we interpolated the GCM data to perfectly fit the solar longitude, latitude and longitude grid of TES observational data. Afterwards we used a simple statistical test to check the differences between the results:

$$z = \frac{|RH_n - RH_d|}{\sqrt{RH_n + RH_d}} \tag{7}$$

where RH_n and RH_d are the RH calculated with nighttime TES measurements together with 2 AM GCM VMR and 2 PM VMR, respectively. Then, we computed yearly average difference by summing up the z differences for each grid point and dividing the sum by the number of data. Comparing these results to the annual averages of RH, the variations are quite considerable. The RH values derived from using

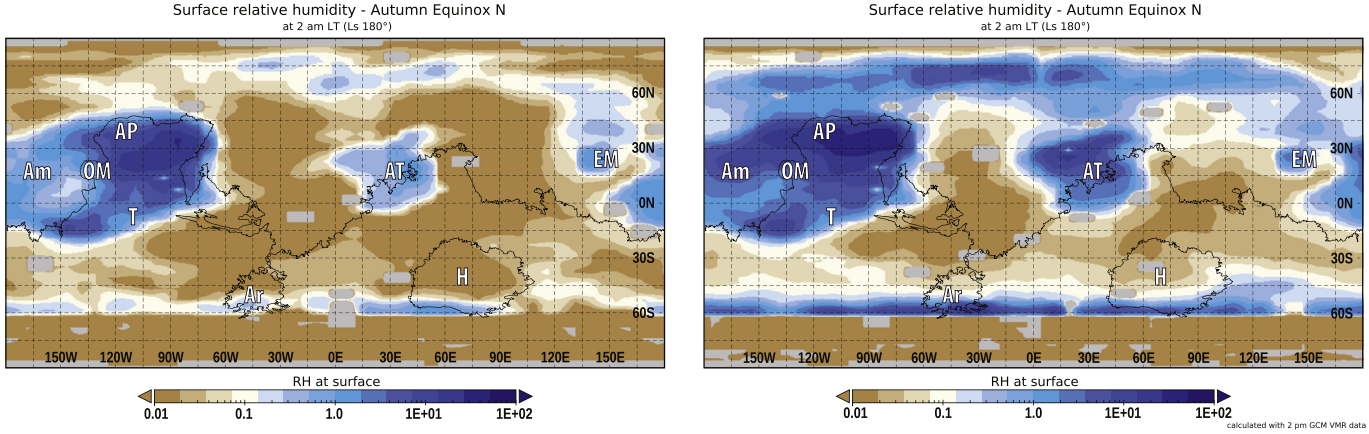

Fig. 2. Differences of near-surface relative humidity if using nighttime or daytime water vapor data. In the left figure the RH calculated with 2 AM TES surface temperature and pressure measurements together with 2 AM GCM VMR values. In the right we coupled the nighttime TES measurements with 2 PM GCM VMR data. It is evident that by using daytime water vapor we overestimate the saturation, but the global distribution of elevated RH regions remains the same.

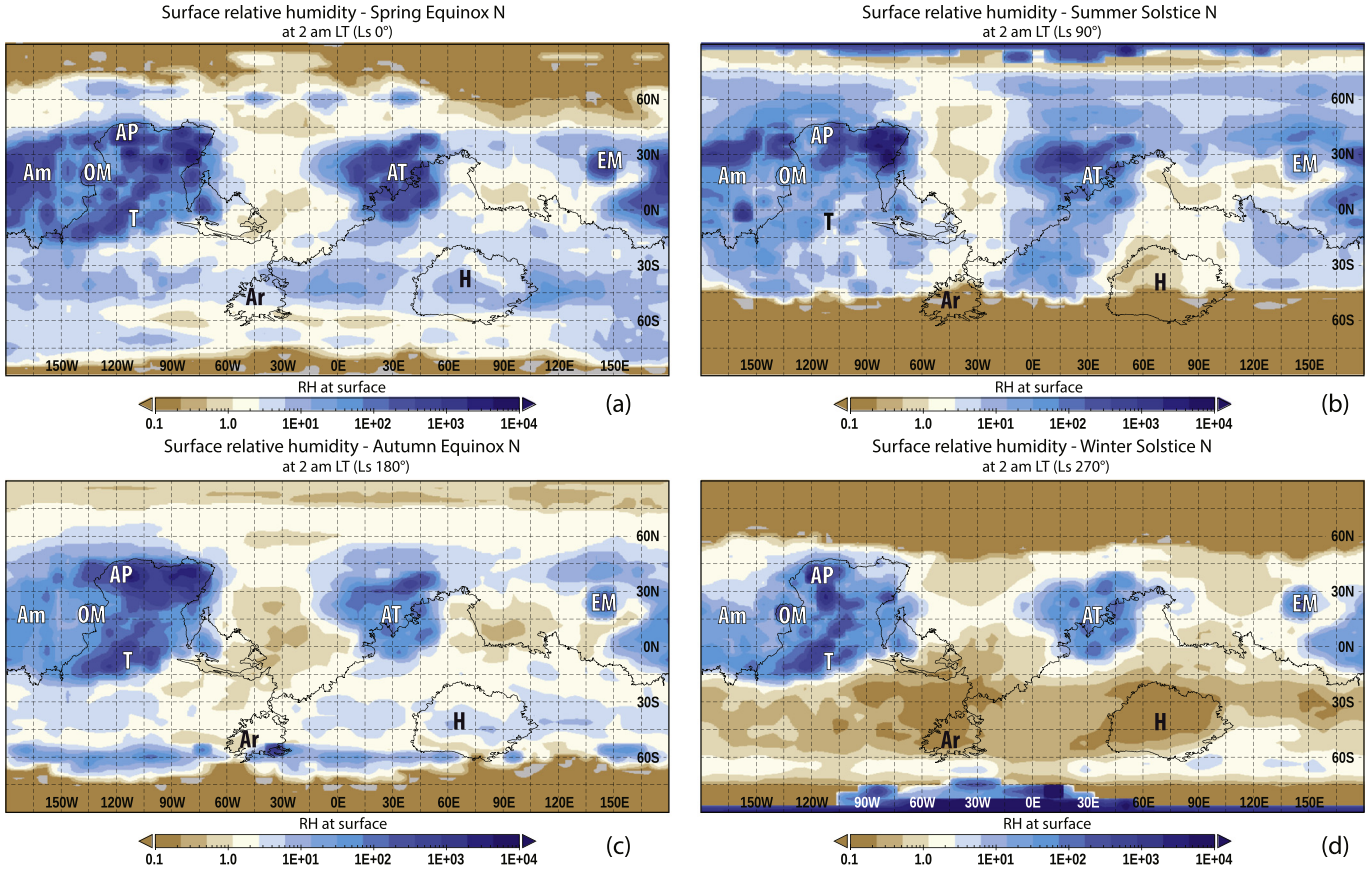

Fig. 3. Seasonal dependence of the nighttime humidity distribution. We derived the relative humidity values directly above the surface from GCM model calculations at the time of northern spring equinox (a), northern summer solstice (b), northern autumn equinox (c) and northern winter solstice (d), 2 AM LT at everywhere on the map. The three humid zones defined in Section 3 are visible in all seasons. They are the least defined during the time of northern summer solstice. During this time the regions south from Tharsis (T), Amazonis (Am) and Arabia Terra (AT) stretch further down south, with similar RH values. The three zones are visible the most clearly during northern winter, at which time their RH values are higher than the rest of the planet surface.

daytime GCM vapor data are consistently higher than the nighttime calculations, however, the overall global distribution is in good agreement as shown in Fig. 2.

For the calculation, we used TES water vapor measurements from 2 PM to calculate the VMR (Q_0) according to Eq. (5), and then determined RH by dividing Q_0 with Q_{sat} (as seen in Eq. (1)) calculated from 2 AM pressure and surface temperature TES measurement data. The idea behind substituting 2 PM water vapor data as an approximation was that surface temperature varies much more than water vapor varies between day and night. More precisely, the change in computed humidity using the observed daytime versus nighttime ST is much greater than the change in computed humidity using the expected daytime versus nighttime water vapor abundance. We realize that water vapor is not the same during the day and night, this is an approximation, however at the present there is no good dataset giving the diurnal variation of water vapor for all seasons over a global scale. Therefore, we have chosen the simplest approximation: that there is no diurnal variation. A diurnal variation of 10–20 %, as in Pankine and Tamppari (2015) would not change any of the main findings of this work, including the location and seasonality of the “humid zones ”. If we look at GCM derived column water vapor, the change from day to night is indeed small (less than 10%).

Fig. 2 shows the differences between near-surface RH calculated with nighttime or daytime GCM vapor data to illustrate the validity of our estimation. On the left the GCM derived 2 AM vapor data coupled with 2 AM TES surface temperature and pressure values, while on the right we used 2 PM GCM vapor data with the nighttime TES measurements. Here, we present only the northern autumn season, but the outcome was the same for each season and TES measurement years. We most likely overestimate the scale of saturation by using daytime water vapor data, but the global distribution of regions showing elevated RH remains the same. The resulting maps are also consistent with the GCM results and TES results presented in the following sections. Since the main goal of this paper is to investigate the global distribution of near-surface relative humidity and its variations between seasons and different geographical regions, we conclude that RH computed from TES this way is valid even with its known limitations and approximations.

3. Results

In the following, we present the resulting figures showing relative humidity, temperature, surface temperature and water vapor volume mixing ratio for the entire planet. In Section 3.1, we show the RH values at the surface derived from the GCM model calculations by presenting 2 AM LT global maps. This local time was selected, because the TES measured the surface temperatures at roughly 2 AM and modelling for the same local times allows us to see global trends and variations coming from two different methods, thus giving us the full picture in greater detail. In these figures, we can examine the seasonal changes excluding daily variations. In Section 3.2 we demonstrate the RH values calculated from nighttime TES measurement data, roughly 2 AM everywhere for the four representative seasons. During all seasons at 2 AM LT on the GCM model results (Section 3.1) three distinct areas appear as oversaturated regions, the first zone being encircled by Amazonis (Am), Alba Patera (AP) and Tharsis (T); the second around Arabia Terra (AT); and the third is the region around Elysium Mons (EM). These are of

course only two zones in reality, but due to their appearance on the maps we refer to them as three for easier identification. We refer to these regions in short as the “humid zones” from now on. Afterwards we present the possible connection the surface thermal inertia in Section 3.3, and investigate the validity of our zones by calculating 4 m data in Section 3.4. In Section 3.5 we examine the global behavior of surface temperature and water vapor mixing ratio, two key elements in calculating the relative humidity, and in the end we discuss the importance of surface properties in Section 3.6 by comparing surface results with 23 m ones.

3.1. GCM results

A certain seasonal change exists in the distribution of RH across the planet, as it is known that the Northern polar cap fills the atmosphere with vapor during the northern summer (Haberle and Jakosky, 1990). The insolation-driven temperatures are related to the varying solar distance, and also differ according to the consequences of the tilt of the rotational axis. For this, we show four representative seasonal phases throughout the Martian year, the northern spring equinox (Ls 0°), summer solstice (Ls 90°), autumn equinox (Ls 180°) and winter solstice (Ls 270°). First, we look at the near-surface RH values at 2 AM LT everywhere on the planet derived from GCM for these different seasons (Fig. 3).

At the northern spring figure (a) the three humid zones defined above are rather apparent in showing generally higher RH values than the rest of the planet. There is also a band, most clearly visible during northern spring and northern autumn between 30° S and 55–60° S, what seems more wet (higher RH) than its vicinity. The polar regions generally seem drier (lower RH) than anywhere else during the northern spring equinox, as water vapor in the atmosphere mainly starts increasing late spring (L_s = 45–90°) in the polar regions as a result of the sublimation of the seasonal ice deposits (Bapst et al., 2015). Comparing the northern spring to autumn, it is overall more humid during spring, excluding the three humid zones, which are more distinct during autumn than in spring. The wet band in the southern hemisphere appears here as well. Compared to the spring season, the northern polar region also has higher RH values during northern autumn.

The figure showing the 2 AM snapshot at the time of the northern summer solstice (Fig. 3b) is quite different from the previous two seasons discussed, spring and autumn. While the three humid zones are there, they are not as well defined as in the other three seasons, and they are more extended. The distinct “crescent moon” -like shape east from EM, and EM is still distinguishable, but the regions around AT and T - Am - AP blend more into their environment. The overall location of the three zones are still the same, but the latter two humid zones stretch more to the north and south than they do in the other seasons. The southern polar region is dry, as the wet band between 30° S and 55–60° S is missing here. During the northern winter on the other hand (Fig. 3d), the three zones are the most isolated in comparison with the other three seasons, and the contrast between the RH values and the environment of the three humid zones appear here the strongest. The apparent “borders” of these regions are well defined with OM and AP being the most humid. The southern pole seems rather wet, which could be the result of the sublimation of the ice during southern summer. Comparing the northern winter and northern summer it seems that the surface of Mars is generally higher in RH during the northern summer, in agreement with the expectations, as the atmospheric vapor is mainly released by the exposed water ice from the northern permanent polar cap.

While we focus on snapshots mostly from 2 AM in this study, it is interesting to take a look at the daily RH trends, and the differences in them between the “humid zones” and other regions. In Fig. 4 are daily RH curves from five representative locations during northern summer solstice (a), and northern autumn equinox (b) derived from GCM calculations. The locations were picked out at the same latitude, in order to minimize variations due to differences in insolation. Three of the five sites are parts of the three humid zones defined in Section 3, AP (30° N 120° W), AT (30° N 30° E) and EM (30° N 150° E). We selected two reference locations, where the RH levels show no significant elevation, at 30° N 30° W and at 30° N 90° E. We see that elevated humidity levels with low temperatures during the night, and daytime dryness with higher temperatures are characteristic of all sites and seasonal periods. Comparing the northern summer solstice (Fig. 4a) with the northern autumn equinox (b), the RH levels are more elevated during the night in autumn at AP and AT. The descending branches of the curves are steeper during autumn. The RH levels generally seem to start decreasing around 4 AM during summer, but they stay elevated until 6 AM in autumn, as the hours exposed to insolation are longer during summer. A similar effect is barely visible on the ascending branch, as the RH levels typically seem to start increasing around 4 PM during both seasons. AP and AT show higher levels by 6 PM in autumn than they do during summer, but there is no significant difference at EM and at the reference locations.

During autumn at AP and AT we observe that the RH levels start increasing around 4 PM and keep rising until 6 AM in the morning. However, during summer they start declining after 10 pm, then strongly decrease after 4 am. During autumn at AP and AT there is another striking feature that the RH levels are the highest during the night. They are the lowest during the day as well — possibly caused by the larger daily temperature fluctuation due to the lower thermal inertia. The same feature is not observable during summer, and the RH levels do not differ as much between AT, AP and the other two locations. At EM and the reference locations there is no significant difference between summer and autumn, aside from the RH levels declining faster during summer morning. Comparing the reference locations to the other three regions the RH levels at 30° N 30° W and 30° N 90° E are changing less in a matter of a day overall, being usually lower during the night, and higher during the day than in the “humid areas ”.

3.2. TES results

The surface RH values calculated from TES data are shown in Fig. 5, approximately 2 AM LT everywhere for the four different seasonal times on Mars. The characteristics of the seasons are similar to what one can see in the data from GCM 2 AM LT (Fig. 3). First, we look at the northern spring equinox in Fig. 5a, where the humid zones defined in Section 3 are rather apparent. Out of these AT, the zone south from Am and the region east from AP show the highest RH values. There also seems to be a wet “band” south from the equator (possibly one of the reasons behind this is the low temperature in that region). However, since the condensation height could not be calculated due to missing water vapor retrieval data south from 55° S, the extent of the elevated RH band cannot be determined. Comparing northern spring to northern summer (Fig. 5b) the distribution of humidity levels is quite similar. The highest RH values show up at approximately the same regions, with the three zones again well defined. Note that there are relatively dry areas between the wet regions at the same latitudinal band, for example between AP and AT locations. This demonstrates that the insolation or distance from the sublimating northern permanent cap is not the dominant influence producing elevated humidity values during the night. There is also indication for the wet “band ”, but because of the missing data in the southern hemisphere, this is only a hint.

The northern autumn (Fig. 5c) and winter (Fig. 5d) figures are again similar to each other. The humid zones appear well defined in both. During autumn the southern hemisphere seems still quite humid, but during northern winter it seems almost completely dry. This latter observation might be related to both that the southern summer is warmer, and that large part of the southern CO_2 cap is permanent. Because of this, the water ice exposure is limited during the local summer, resulting in an overall smaller contribution to the water vapor levels. In general, these are in good agreement with the GCM results shown in the

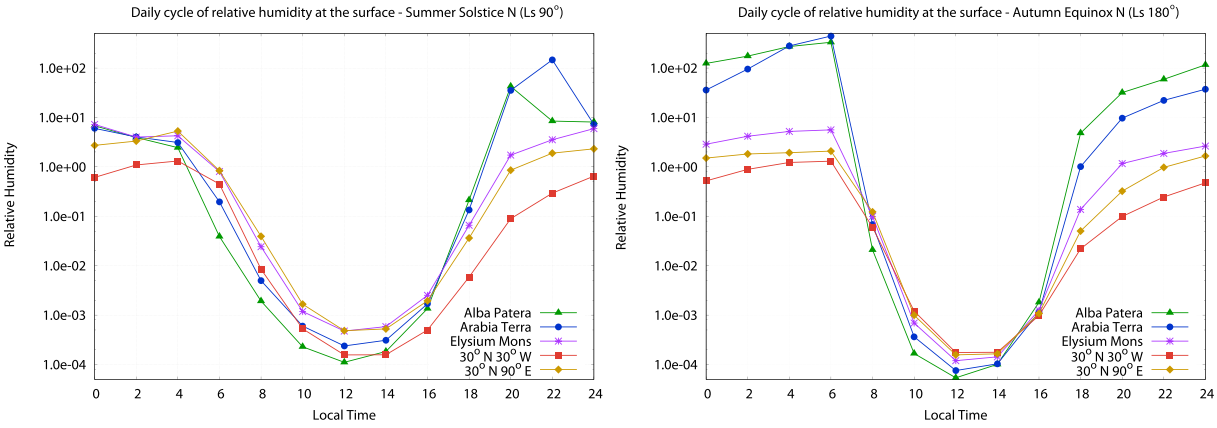

Fig. 4. Daily cycles of near-surface humidity at the time of northern summer solstice and northern autumn equinox at Sol 195 (northern summer solstice - Ls 90) and at Sol 373 (northern autumn aquinox - Ls 180) calculated from GCM data. The five locations examined are Alba Patera (30° N 120° W), Arabia Terra (30° N 30° E), Elysium Mons (30° N 150° E) from the three previously defined humid zones, and two reference locations outside these humid zones, one located at 30° N 30° W and the other at 30° N 90° E.

previous sections, especially related to the location of the humid areas.

3.3. Relation to thermal inertia

Thermal inertia (TI) is one of the most important elements of diurnal temperature variations at the surface of Mars. It changes with particle size, rock abundance, degree of induration and exposure of bedrock within the top few centimeters of the subsurface. TI provides a measure of the ability of the subsurface to store heat during the day and re-radiate it during the night (Putzig et al., 2005). On the basis of TI values one can effectively estimate the grain sizes. Relatively higher TI values (~ 400 $Jm^{-2}K^{-1}s^{-1/2}$) indicate coarser material, while lower values (~ 250 $Jm^{-2}K^{-1}s^{-1/2}$) suggest fine grained particles like sand or dust (~ 20–100 $Jm^{-2}K^{-1}s^{-1/2}$). The temperature of a material with

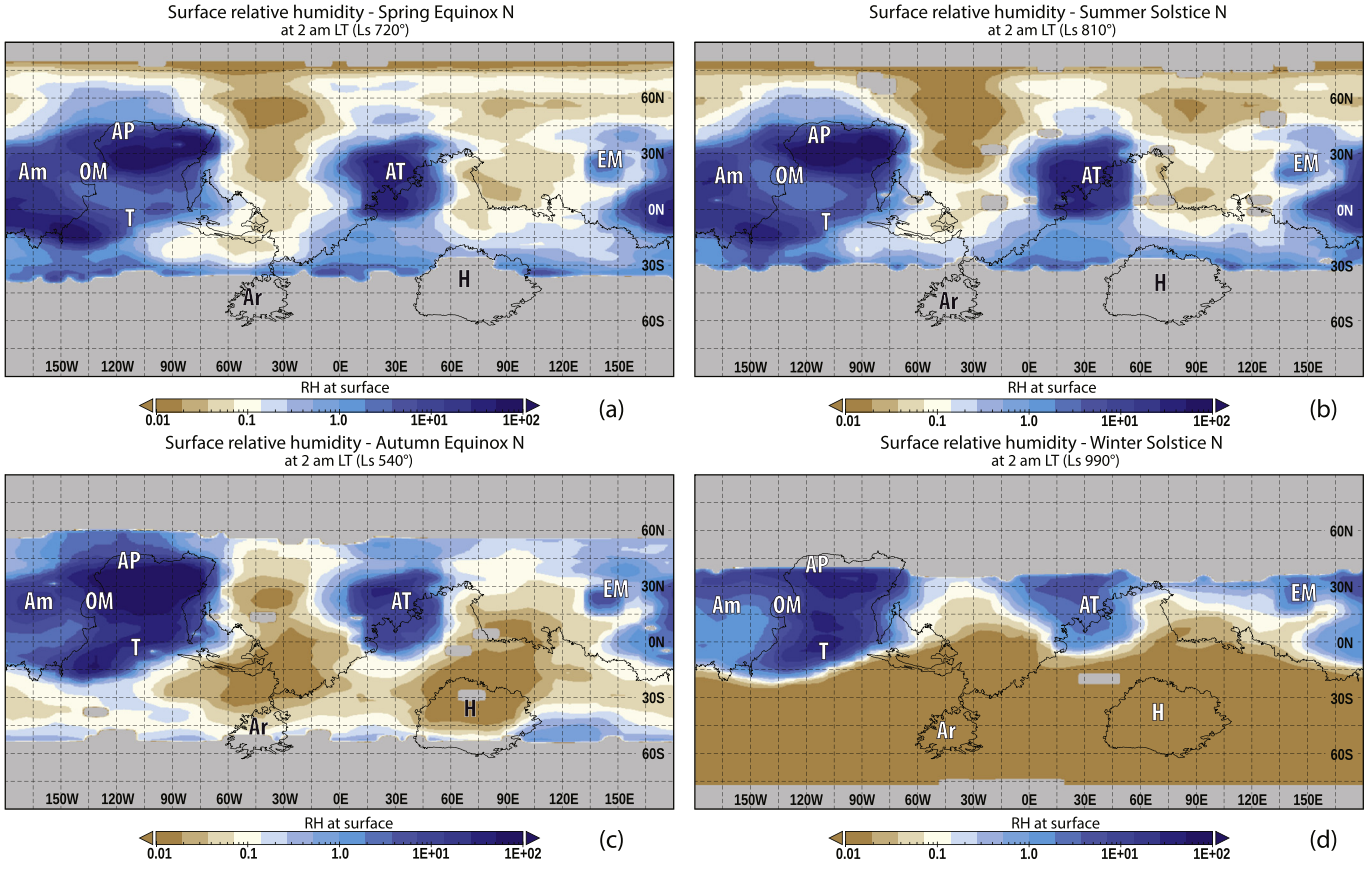

Fig. 5. Seasonal dependence of the nighttime humidity distribution. We derived the RH values from TES measurement data at the time of the northern spring equinox (a), northern summer solstice (b), northern autumn equinox (c) and northern winter solstice (d). The measured temperature and pressure data came from approximately 2 AM LT, while the TES water vapor measurements were collected at approximately 2 PM. The three humid zones defined in Section 3 are visible here as well. The regions showing the highest RH values are east from Alba Patera (AP) and around Arabia Terra (AT). These areas have higher RH values, than the other regions of the humid zones, and compared to the dry sectors the RH values ar even higher. The gray areas in the figures correspond to places where RH could not be calculated due to missing water vapor retrieval data.

low TI values varies significantly during the day, while the change is not as drastic in the case of materials with higher TI. In[1] Fig. 6 there are 3 distinct areas which have characteristically lower TI values than their surroundings. One is roughly between -10° E — 60° E, 5° S — 35° N, one is approximately between -60° E — 150° E, 25° S — 60° N, with a smaller region centered around 145° E, Elysium Mons. The third zone located below 60° S, and can be seen on all longitudes.

The first two regions (AP-OM-T and AT) in the northern hemisphere, and close to the equator shown in the TI map seem to be relatively in sync with the "humid" zones observed in the TES and GCM 2 AM maps. According to the research of Putzig et al. (2005) these regions located mostly in the northern hemisphere are of low TI and high albedo, interpreted as surfaces dominated by unconsolidated fines (dust with grain sizes less than ~ 40 μm). As for the band in the southern hemisphere, the surface is covered by material with relatively low TI and low albedo, comparable of the areas with TI around 300 $Jm^{-2}K^{-1}s^{-1/2}$. Normally such low TI values would suggest a surface of unconsolidated, fine-grained dust, such as the northern regions are believed to be, but because of the low albedo Putzig et al. (2005) propose a different explanation: they conclude that a low-density mantle formed by desiccation of a previously ice-rich near-surface layer is the most likely explanation for the observed properties. This is a phenomenon analogous to those which produce terrestrial low-density soils such as the desiccation of ice-cemented loess (Johnson and Lorenz, 2000).

3.4. Relative humidity at approximately 4 m

We emphasize we were substituting the ≈ 4 m VMR for the near-surface values. In order to confirm that the elevation of RH is not an artifact coming from this simplification, we examined the RH distribution calculated with the approx. 4 m GCM temperature, water vapor volume mixing ratio and pressure data.

In Fig. 7 the "humid zones" appear most clearly around the northern autumn, but they show elevation at all seasons. Their southern "borders" are especially clear at the northern winter solstice. According to the approximately 4 m height calculations, the variation seems the smallest during the northern summer, where the zones northern and southern edges are rather non-existent. The regions only appear to be separated by the drier zone around 30 W. The RH values are lower than the calculations at the surface as expected, however the oversaturation above low TI regions is visible in the 4 m data as well. We conclude that the elevated humidities do not appear solely in the surface calculations.

3.5. Surface temperature and water vapor behavior

As the calculated RH depends on T, P and VMR, it is important to examine the characteristics of these parameters in understanding the global variations. While the SP values do change throughout the seasons, there is no global distribution variation similar to the ST and VMR changes. Therefore, in the following we will focus on the latter two parameters. First we look at the global characteristics of ST during the night. Fig. 8 depicts the GCM ST values at 2 AM LT everywhere on the planet, at the time of the northern summer solstice on the left (a), and northern autumn equinox on the right (b). In these figures three distinct areas in the northern hemisphere (Am-OM-AP, AT and EM) have approximately 30-degree lower temperatures than their environment. These three zones correspond to the three humid zones defined in Section 3. During summer the area east of Alba Patera, and the region west from Tharsis seems to be the coldest of these three zones.

At the time of northern summer these zones are similar in temperature to the southern hemisphere, where there is currently winter. During northern winter the coldest regions seems to be around Olympus Mons and Alba Patera. The difference in insolation is also observable that in the northern autumn the equatorial region is the warmest at night. However, the three zones show little, only around 5–10 K variation in their temperature. This is still valid for the other two seasons not shown here, Ls 0° and Ls 270°. We can conclude that these zones are consistently colder at 2 am, therefore cool down during the night at any season throughout the Martian year.

Fig. 9 illustrates the GCM VMR snapshot from 2 AM LT at approximately 4 m above the surface, with the northern summer solstice on the left (a) and the autumn equinox on the right (b). The three zones introduced in Section 3 are visible here as regions where the VMR is lower than elsewhere in the northern hemisphere at the time, e.g. there is less water vapor in the near-surface atmospheric layers above these regions. The exceptions are Olympus Mons, Tharsis Montes and Elysium Mons, which show higher values than the rest of the "humid zones ". During the northern autumn shown in Fig. 9b, the three zones appear as rather vapor-poor areas as well, showing values of around 10^{-5} mol/mol, while it is roughly an order of magnitude lower during summer. The regions around Olympus Mons, Tharsis Montes and Elysium Mons are again showing higher VMR values, with Tharsis Montes more defined here than during summer. This correlation with surface pressure (topography) have also been observed previously, and it might still be true after the topography has been "removed ", because the water vapor is not well-mixed through the entire atmosphere (Smith, 2002). For example, the Phoenix results indicated that a large amount of water must be confined to the lowest 0.5–1 km (Tamppari and Lemmon, 2016). From the TES observations we find that a steep latitudinal gradient forms during aphelion season high in the north in water vapor abundance, while during the perihelion the water vapor is more uniformly spread out (Smith, 2002). This phenomenon is observable here with the northern polar and high latitude regions showing higher VMR values than the equatorial regions at the time of the northern summer solstice (9a). The northern summer is characterized by a gradual southward transport of sublimed water from the northern polar cap to the equatorial regions (Steele et al., 2014). By the time of the northern autumn equinox (9b) water vapor reaches peak values around the equator, corresponding to travel via Hadley cell circulation.

To further examine the possible processes, we investigated the daily variations of near-surface VMR at five representative locations at the same latitude to rule out seasonal effects, the same ones as describe before. The "humid" regions cool down more quickly during the night than the ones with higher TI values. By examining the changes in VMR at approximately 4 m above the surface, one can see in the GCM Fig. 10 that the VMR values drop above the "humid" areas during the night. If we look at the available water vapor with respect to the elevation (Fig. 11, GCM) it is clear that there is a depletion of water vapor near the surface at night.

To investigate whether the daily cycle of VMR shown in Fig. 10 is indeed a global behavior and the depletion seen in Fig. 11 is a global phenomenon at other times than 2 AM as well, we included maps at two other representative local times.

Figs. 12 and 13 depict the changes of 4 m VMR values in a global scale from GCM. The depletion of vapor during the night shown in Fig. 11 is evident not only in the daily curves (Fig. 10), but looking at the whole near-surface of Mars as well. From the daily variations we have chosen 9 AM LT and 8 PM LT to represent the global changes, since by 9 AM the VMR levels rise to their daytime values, and by 8 PM they start decreasing down at all locations investigated in Fig. 10. At 9 AM the water vapor at 4 m is mostly homogeneous in distribution with values reaching 1.6×10^{-4} mol/mol excluding the polar regions at the autumn equinox, and most of the southern hemisphere during the northern summer solstice. The vapor distribution does not change much during the daytime. As the night comes the vapor levels starts decreasing and Fig. 13 shows that VMR drops more quickly above the low

[1] Data came from: Putzig, N.E., M.T. Mellon, T.L. Heet, and J.G. Ward, MGS Mars TES Derived Thermal Inertia Maps V1.0, MGS-M-TES-5-TIMAP-V1.0, NASA Planetary Data System, 2009., the map was created by V. Steinmann.

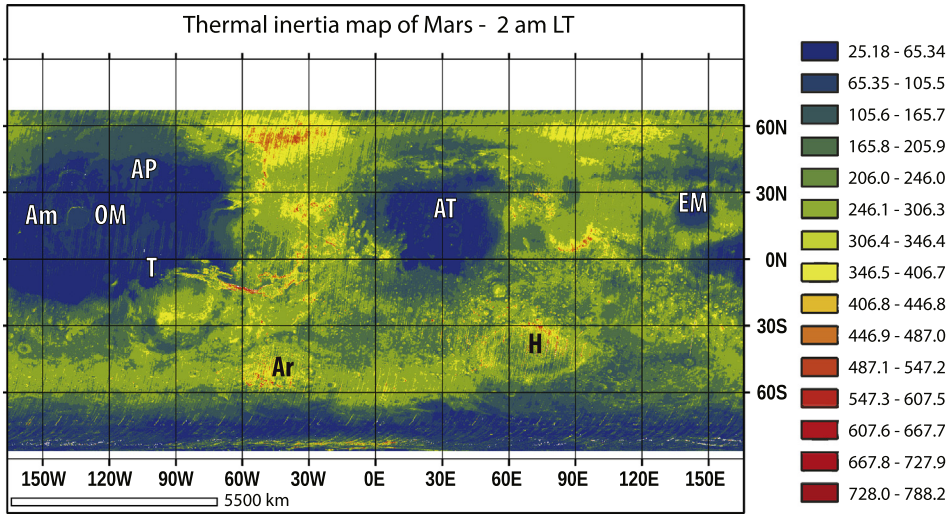

Fig. 6. Thermal Inertia data at night measured by TES. The three zones defined in Section 3.1 are visible here as low TI zones. The low TI area around Elysium Mons, as well as the slightly higher, but still low TI region north from there are also distinct and form the same specific shape resembling a crescent moon, as seen in the previous VMR, ST and RH figures.

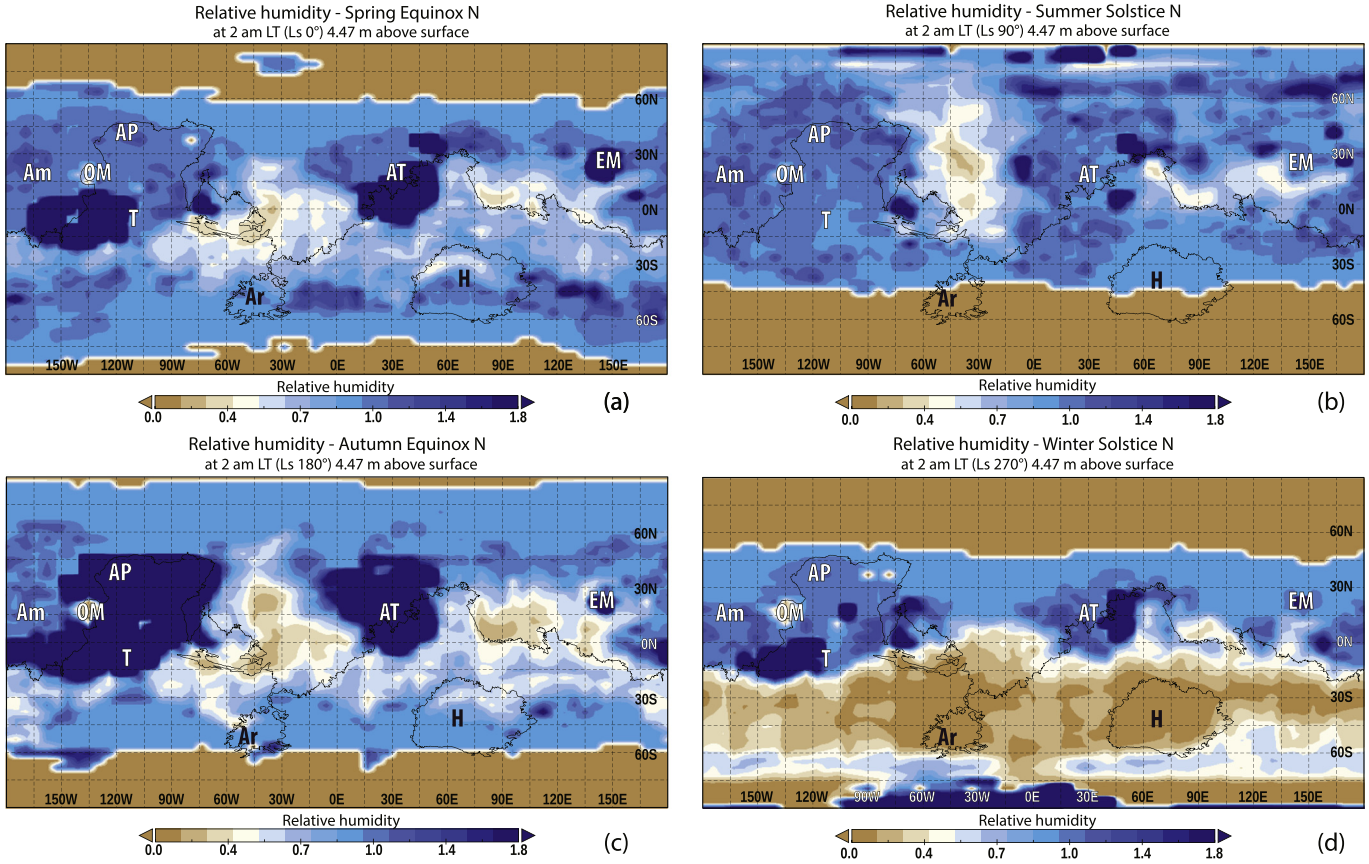

Fig. 7. Seasonal variation of RH distribution at approximately 4 m above the surface derived from GCM data. The "humid" zones appear less clearly, but the elevated RH values are visible at the low TI regions at every season, especially at the time of the northern autumn equinox. Thus we conclude that the appearance of elevated near-surface RH is not due solely to our approximation and way of calculation.

TI "humid zones ". While the same difference in VMR is not that obvious at the time of the northern summer solstice due to the overall higher daytime VMR levels, compared to the 9 AM figures, the amount of vapor decreases in the lower atmosphere. This suggests exchange processes with the surface in the form of condensation or adsorption onto the grains. Comparing all the water vapor figures at 4 m, VMR drops during the night to around 1.2×10^{-6} mol/mol by 6 AM, and lowers more quickly above the "humid zones ".

3.6. *The importance of surface properties*

In Fig. 14, the RH calculated from GCM values is shown, approximately 23 m above the surface. We investigated the RH at this height to see how much variation a ~ 20 m difference causes. Looking at the results, the distribution of RH can be quite different close to the surface, as expected. The global "trend" is somewhat similar to what we have seen in the GCM near-surface RH figures (Fig. 3). The southern summer is drier (lower RH) than the northern summer, showing the kind of hemispherical asymmetry as previously described in for example

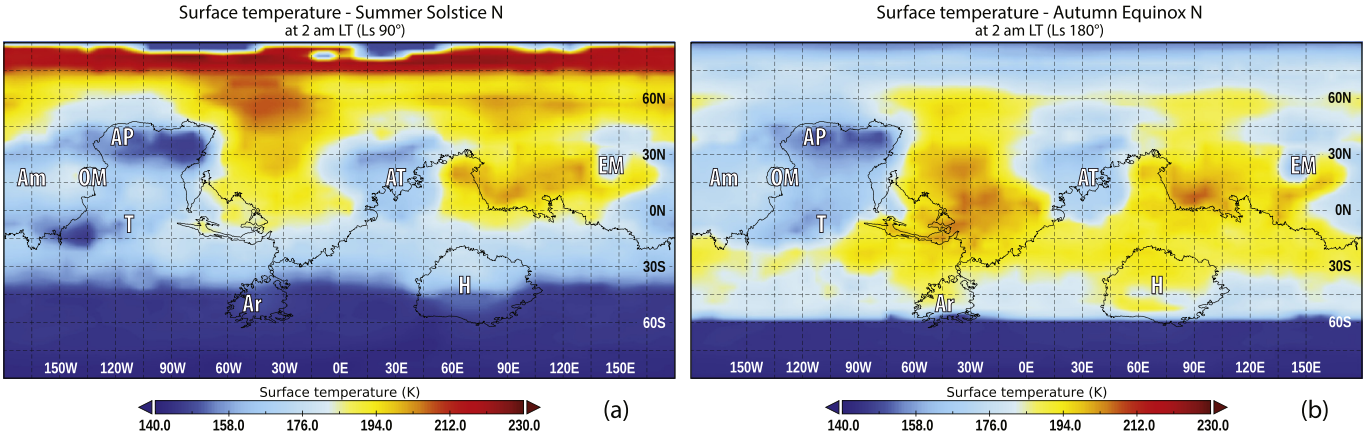

Fig. 8. Seasonal dependence of the nighttime surface temperatures data from GCM at the time of the northern summer solstice (a) and northern autumn equinox (b), at 2 AM LT everywhere. The three "humid" zones defined in Section 3 are apparent here, which are colder than their surroundings with temperatures ranging from ≈ 140 K to ≈ 175 K. The area east of Alba Patera (AP) seem to be the coldest part of these three zones, showing temperatures around ≈ 140 K.

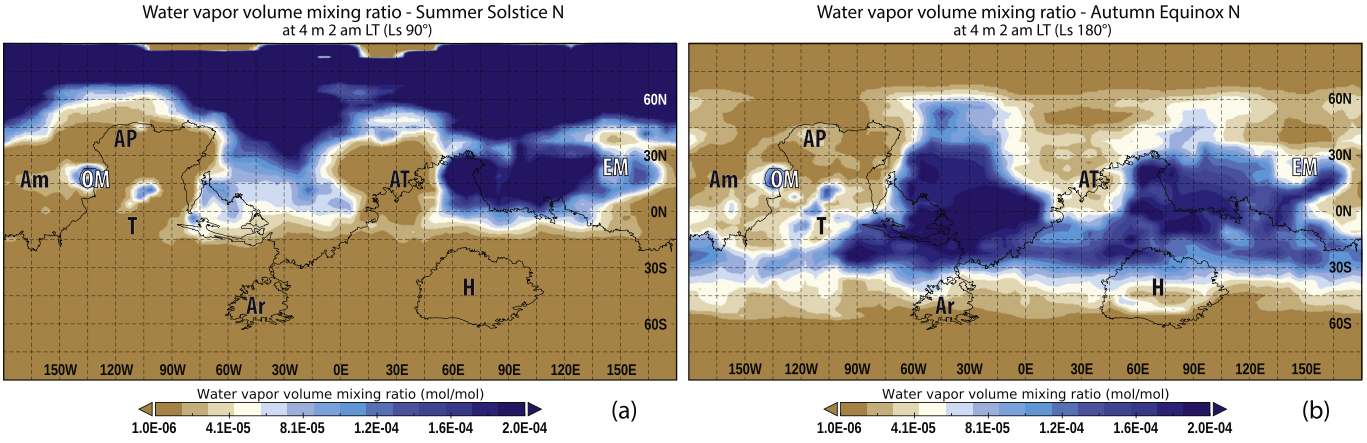

Fig. 9. Seasonal dependence of water vapor volume mixing ratio data from GCM at the northern summer solstice (a) and northern autumn equinox (b) at approximately 4 m above surface, 2 AM LT globally. The three humid zones defined in Section 3 appear here as regions, where the VMR is approximately 3 orders of magnitude lower than their surroundings. The exceptions are Olympus Mons (OM), Tharsis Montes (northwest from Tharsis denoted by T), and Elysium Mons (EM). These mountains show 1–2 orders of magnitude higher VMR values than the rest of the humid zones. We can also observe that during northern summer the southern borders of these zones are not defined, with the exception of Arabia Terra (AT). During northern autumn the northern boundaries blend together with the northern polar region. This shows a trend of higher VMR values moving to the south as the seasons change from summer to eventually winter in the northern hemisphere (Smith, 2002; Steele et al., 2014).

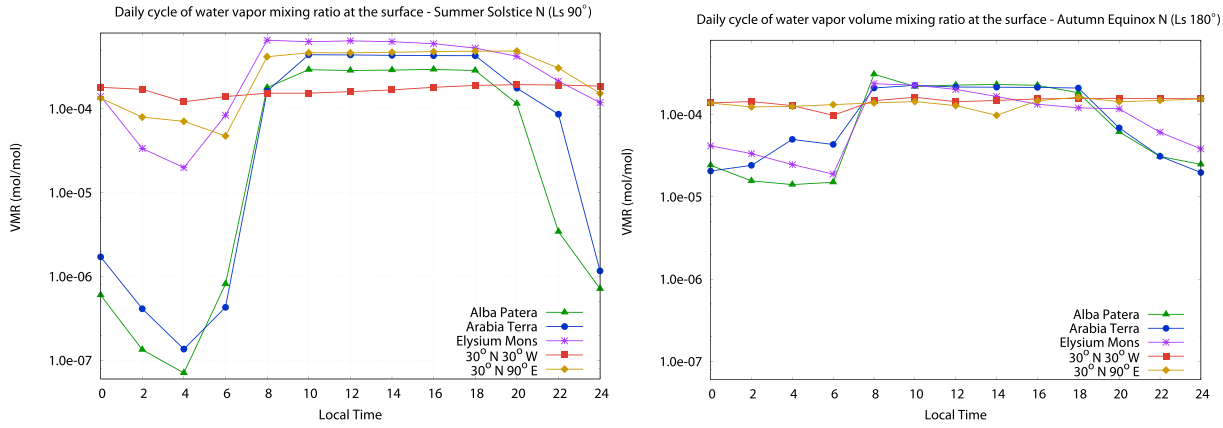

Fig. 10. Daily curves of VMR at the time of the northern summer solstice (left) and the northern autumn equinox (right) from the GCM data. The locations are Alba Patera, Arabia Terra, Elysium Mons and two reference "dry" locations, one at 30° N 30° W, and the other at 30° N 90° E. All selected analyzed points are located at latitude 30° N to exclude different seasonal effects. The two reference "dry" regions show smaller fluctuations throughout the day in both seasons.

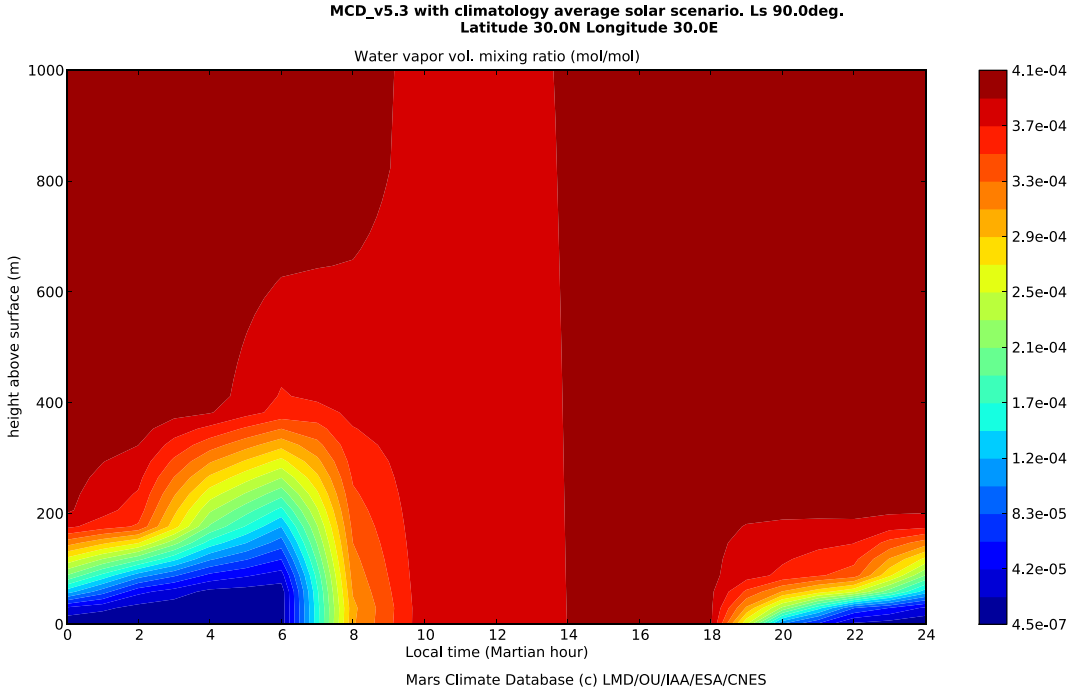

Fig. 11. Daily variation of GCM derived VMR with altitude at Alba Patera (30° N 0° E). A depletion is visible in the lower ranges of the atmosphere reaching the lowest values below 70 m. The VMR is lowest between 8 PM and 6 AM.

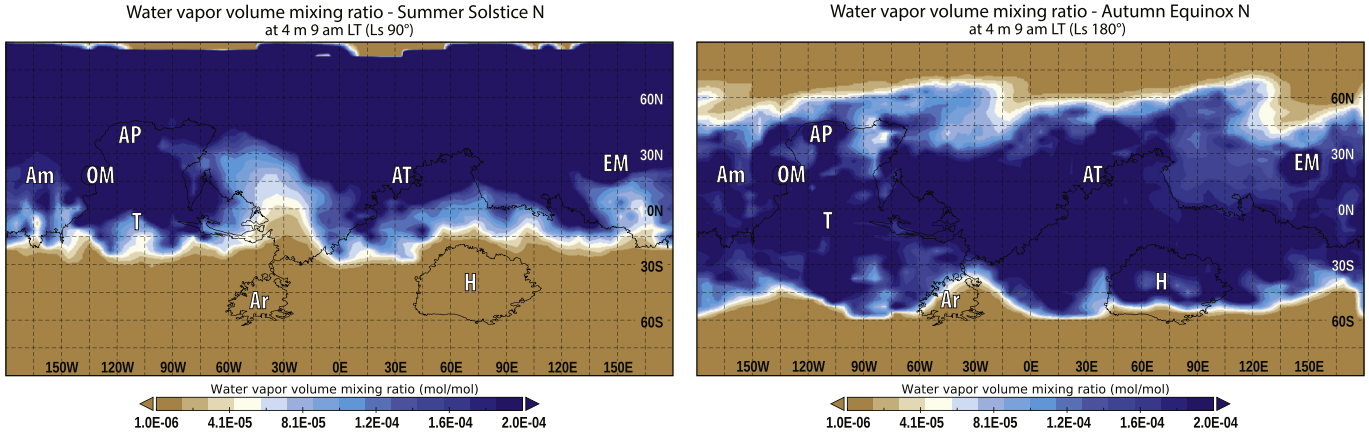

Fig. 12. Global distribution of VMR at 9 AM LT derived from GCM at the time of the northern summer solstice (left) and northern autumn equinox (right). According to the daily curves, the VMR returns to the daytime levels by this time. In the map one can see, that indeed the water vapor above the surface is mostly continuous in distribution with values around 1.6×10^{-4} mol/mol in both seasons presented here.

Jakosky and Farmer (1982), Smith (2002), Tokano (2005).There are slightly higher RH values at the presumed "humid" regions during the northern summer, and at the time of the northern autumn equinox 2 of the 3 humid zones appear partially, the RH levels are much lower, than at the surface, as expected. In Fig. 15 the T values modelled with GCM at approximately 23 m above the surface are depicted at 2 AM LT, at the time of northern summer (a) and northern autumn (b). In these T maps the three humid zones defined in Section 3 are still visible, but the differences between these regions and their surroundings are less notable. Comparing these figures with the aforementioned Fig. 14, the substantial role of near-surface effects (mainly the low thermal inertia produced strong cooling and related condensation or adsorption onto the grains) in the behavior of relative humidity at the surface is apparent. This effect could be further strengthened by the occurrence of hygroscopic materials in the regolith, that are able to trap the H_2O much below saturation level (Gough et al., 2016; Robertson and Bish, 2011).

In Fig. 16 the GCM VMR is shown at approximately 23 m above the surface. In Fig. 16a. there is a 2 AM snapshot at the time of the northern summer solstice, and in Fig. 16b. at the time of the northern autumn equinox. The three humid zones defined in Section 3 show up here as areas, where the VMR levels are lower than in their environment, with the exception of Olympus Mons (OM), Tharsis Montes (northwest from Tharsis denoted by T) and Elysium Mons (EM). Comparing the resulting VMR figures at 23 m high with the values modelled at the near-surface (Fig. 9), there is no significant variation. The difference in values between the T, P or VMR at the surface and at 23 m above does not explain the magnitude of variation between the surface (Fig. 3) and 23 m (Fig. 14) in the global RH maps. Thus we conclude that TI and other regolith properties e.g. condensation and adsorption on grain surfaces likely play a significant role in determining near-surface RH levels.

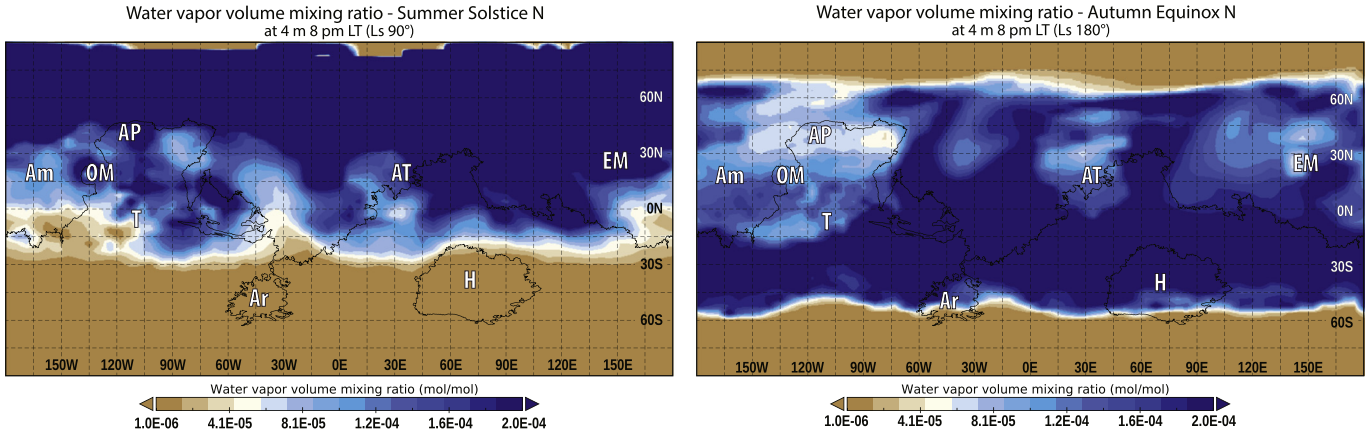

Fig. 13. Global distribution of VMR at 8 PM LT derived from GCM at the time of the northern summer solstice (left) and northern autumn equinox (right). The daily curves show, that at 8 PM the water vapor levels start reducing, but do not reach the minimum values yet. The vapor level gets lower to around 1.0×10^{-4} mol/mol above Am - AP - T, AT and in the vicinity of EM as well, while in other areas it mostly stays above 1.6×10^{-4} mol/mol at the northern autumn equinox. The appearance of the "humid zones" is less clear at the northern summer solstice due to the overall higher daytime VMR in summer falling under 1.0×10^{-4} mol/mol approximately 1 h later.

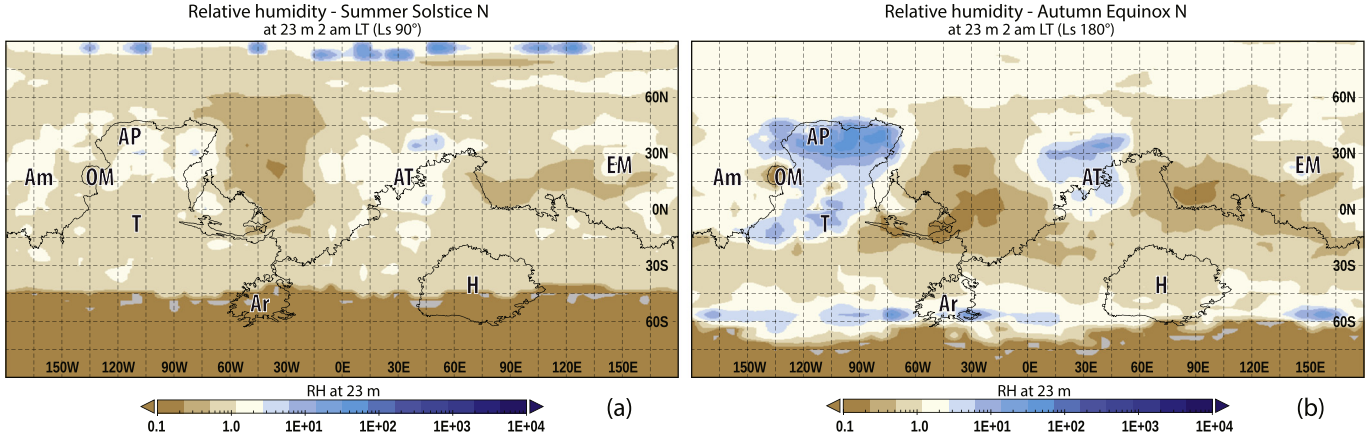

Fig. 14. Seasonal dependence of nighttime RH distribution at 23 m above the surface from GCM model calculations. Local time is 2 AM globally at the time of northern summer solstice (a) and northern autumn equinox (b). The southern elevated RH band appears although discontinuously, out of the 3 humid zones defined in Section 3 only 2 appear, and only partially. We can also note the area between 60° W and 15° W with lower RH values during northern summer. This is the same area, which was visible at the previous RH figures, and also appears partially during the autumn equinox.

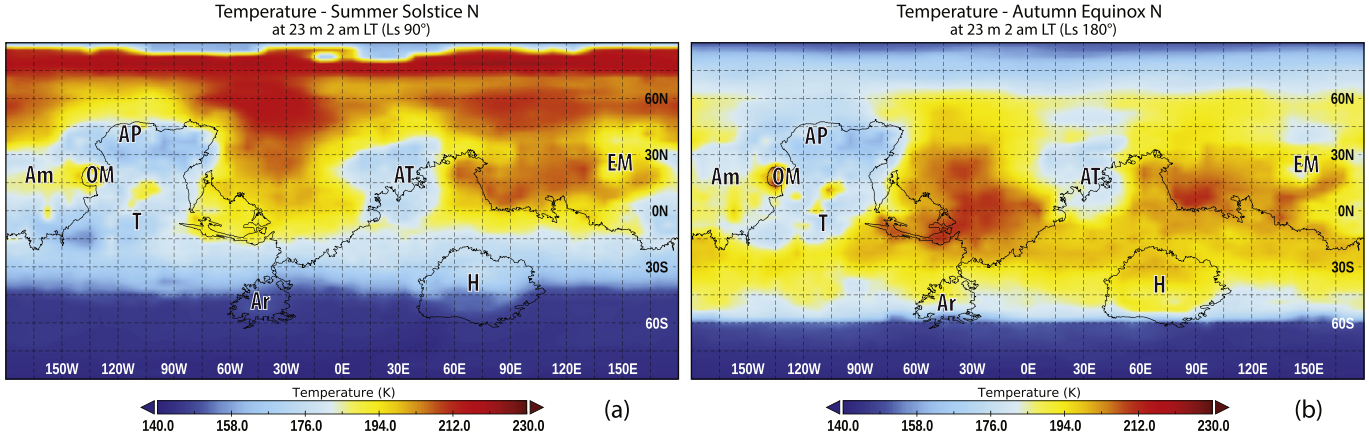

Fig. 15. Seasonal dependence of nighttime T from GCM data at approximately 23 m above the surface at the time of northern summer solstice (a) and northern autumn equinox (b). Local time is 2 AM at the whole planet. The three humid zones defined in Section 3 are still identifiable here, but the contrast between the temperatures here and their warmer environment is less significant. Compared with the surface data it is overall warmer during all seasons.

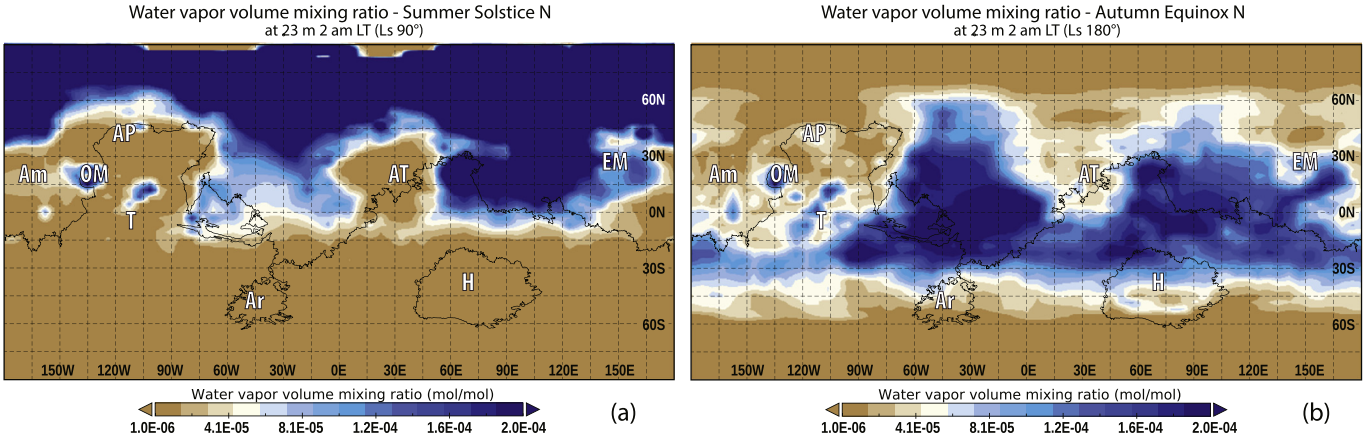

Fig. 16. Seasonal dependence of VMR at approximately 23 m above the surface from GCM model calculations. The local time is 2 AM globally at northern summer solstice (a) and northern autumn equinox (b). The three humid zones defined in Section 3 are visible here as well. Comparing these figures with the ones 4 m above the surface (Fig. 9) there are no considerable differences.

4. Discussion

We have found three areas on Mars where the RH levels are elevated, potentially supersaturated regardless of season. Our findings of high RH, low water vapor bearing areas coinciding with regions showing low TI and high albedo values is in good agreement with previous research in Martian near-surface and subsurface water content studies: Rivera-Valentín et al. (2018) show, that the shallow subsurface for terrains with low TI ($\Gamma \lesssim 300 \mathrm{Jm}^{-2}\mathrm{K}^{-1}\mathrm{s}^{-1/2}$) may be occasionally favorable to brine formation through deliquescence, and the localization of elevated relative humidity regions agree quite well when comparing the maps of seasonally averaged water vapor column abundance maps shown in Smith (2002), Tokano (2003). These “humid zones” cool down strongly, which leads to the possible oversaturation making them interesting in relation to deliquescence processes. Low TI values, beside causing strong cooling and oversaturation, also suggest very fine soil particles with high specific surface area, which may enhance the adsorbing ability of these regions due to a larger adsorptive capacity (Tokano, 2003). The “humid zones" we identified are also in good agreement with the potential solubility of O_2 in brines (especially containing perchlorates) across the Martian near-surface (Stamenković et al., 2018). The Tharsis region and Arabia Terra have been also previously identified as possibly containing higher amounts of adsorbed water (Tokano, 2003). Considering the low nightly ST shown in Fig. 8 and the drop in the water vapor content above the surface (Fig. 10), this suggests a diurnal subsurface exchange. For example, during the night water vapor condenses on the surface or is also (or exclusively) adsorbed onto the grains (Moores et al., 2011; Tamppari and Lemmon, 2016; Whiteway et al., 2009).

Currently the largest seasonal source of atmospheric water on Mars comes from the sublimation of the H_2O polar caps in summer (Bass and Paige, 2000; Richardson and Wilson, 2002). The sublimation of the northern polar cap begins around late northern spring, and continues throughout northern summer. During this season the sublimed water vapor gradually gets transferred from the polar regions towards the equator. Towards the end of the season, water vapor gets transferred from the southern hemisphere northwards, and in the northern hemisphere southwards because of the changing mean meridional circulation, however the net transport is still southward (Steele et al., 2014). This process can be seen in the RH maps (Figs. 3 and 5) with the RH levels rising as we move towards northern autumn. The main transport routes are Arabia Terra and Tharsis (Steele et al., 2014), which regions are also parts of the three “humid” zones defined previously. As we reach the northern autumn equinox, in the RH figures we can observe a band at 50° S latitude, where it is more humid, than elsewhere in the vicinity. There is also another humid band at 60° S latitude, where RH levels are even higher, probably associated with transient eddies and the increased water vapor supply as the seasonal ice deposits around the southern pole also begin to sublime. A similar effect can be seen at 60° N latitude during northern spring and summer. The south pole reaches its maximum water vapor column value around the time of the northern winter solstice, Ls 270°. There is some elevation in RH levels during this time in the southern hemisphere, but compared to the other seasons, the regions south from 15° S are dry. This could be the consequence of the intensifying southern hemisphere Hadley cell, which leads to transport from the southern polar area towards the winter hemisphere being limited. This together with the lower temperatures cause water vapor to recondense back onto the southern pole. As can be seen in the RH figures, by the time of the northern spring equinox the majority of the water vapor is again mostly restricted to the mid-latitudes, with transient eddies being responsible for transport polewards from 45° (Steele et al., 2014).

Our work concentrated on the global distribution of elevated near-surface RH values and their seasonal behavior. Because of the complexity of modelling the surface-atmosphere interactions, the model-based assumption of VMR is currently not reliable under 4 m above the surface. Assuming the water vapor to be well-mixed between the surface and 4 m is a good estimate, but due to comparing atmospheric vapor values with surface temperature data, the numerical values can reach unrealistically high saturation levels in some locations. The nighttime atmosphere is much warmer than the surface, especially above regions covered with low TI bearing materials, and just near it the atmosphere is drier due to the interaction with the surface. Our work shows a “potential supersaturation” and while the specific numerical values may not be accurate in all instances, the distribution of elevated RH is reliable and gives a good estimate even with its known limitations. This study could be useful to study the global behavior of near-surface RH and the role of TI in it, and also to provide a base in choosing future sites of interest in relation to for example, deliquescence processes. At the identified “humid” zones the surface condensation of H_2O is enhanced, therefore nighttime frost formation is more likely than at other locations at the same latitudes. The process of deliquescence is also more probable, and due to the grain sizes adsorption is enhanced as well at these regions. Thus their further analysis related to the potential of liquid water or brine formation and the occurrence of hygroscopic minerals there is important.

5. Conclusion

We investigated the global seasonal and daily variations of near-

surface RH on Mars using calculations from modelled and measured data. We mostly focused on snapshots during the night, particularly approximately 2 AM everywhere on the planet. The reason behind this was to eliminate daily effects related to differences in insolation, and to be able to compare RH derived from LMDZ GCM model calculations with values calculated from TES measurements. We mainly focused on global effects, but also touched upon the subject of daily variations of RH and VMR for illustration purposes.

We identified three “humid” zones, which show elevated RH levels compared to other areas during nighttime regardless of season, with certain variations discussed in detail in the results section. The term “humid” refers to the RH levels being higher than in their vicinity around 2 AM LT, although it does not necessarily mean that there is a large mass of water in the atmosphere. These three areas are regions on Mars, where the TI is low and the albedo is high, which suggest that they are covered by unconsolidated fine dust with grain sizes smaller than ~ 40 μm. As a result they show larger temperature variations throughout a day, cool down more quickly during the night and heat up more rapidly during the day. This effect can be seen on the 2 AM LT maps, where the “humid ” zones show 20–70 K lower temperatures than their surroundings. Above these areas the VMR drops quickly during the night. The difference in values either between the ST and ~ 23 m high T or the ~ 4 m high and ~ 23 m VMR does not explain the magnitude of variation seen comparing the near-surface RH and ~ 23 m RH levels. At ~ 23 m above the surface mainly the zonal and meridional circulation patterns dominate the distribution of RH values, with little variation in connection to TI of the surface. For this we conclude, that TI could play an important role in the changes of near-surface RH, and in the overall humidity evolution of the atmospheric layers very close to the surface. As the water vapor levels drop near-surface during the night, we suggest that some kind of condensation of water vapor could occur during the night supported by the elevated relative humidity here in the form of brines, wettening the fine grains by adsorption or deliquescence. These findings confirm that surface TI dominate the locations of nighttime condensation below the planetary boundary layer and causes a visible decrease in the atmospheric H_2O mass there. This process could influence the global daily H_2O exchange in the very shallow regions of the regolith and may be examined by in-situ measurements according to the locations and periods when and where the probability of H_2O condensation is the highest. Examining the daily RH curves at the three “humid” zones and two reference “dry” zones, the RH values are higher during the night and lower during the day at Alba Patera and Arabia Terra locations. Elysium Mons also shows higher nightly and lower daily RH values, but the difference to the reference areas is not that substantial. A more detailed investigation of the daily variations will be a part of our future research in near-surface RH. Precisely modelling and predicting humidity of near-surface layers of Mars is not a trivial task, but we believe that our work is reasonable and could be useful in planning of future research in the topic of recent possibility of liquid water on Mars.

Acknowledgement

This work was funded by the COOP-NN-116927 project of NKFIH, EXODRILTECH (4000119270) project, the GINOP-2.3.2-15-2016-00003 grant of the National Research, Development and Innovation Office (NKFIH, Hungary) and the TD1308 *Origins and evolution of life on Earth and in the Universe* COST actions numbers 39045 and 39078. Special thanks to Vladimir V. Zakharov for his invaluable help with the NetCDF file handling. The NetCDF files were visualized with the NASA GISS Panoply viewer developed by Dr. Robert B. Schmunk. The thermal inertia map (Fig. 6.) was created by Vilmos Steinmann. Special thank you for Gerard Willinger and László Szabados for the improvement of the language of the manuscript. We also thank the referees for their valuable input which have greatly improved this manuscript.

Appendix A. TES VMR calculation

To obtain the water vapor mixing ratio, we divided the number of H_2O molecules per cm^2 in an atmospheric column by the number of CO_2 molecules per column. This is an approximation, but since roughly 95% of the Martian atmosphere is composed of carbon dioxide, this assumption is reasonable. The number of CO_2 molecules can be calculated by dividing the mass of CO_2 per cm^2 by the mass of a single molecule:

$$n_{CO_2} = \frac{m_{CO_2}}{44 \times 1.66 \times 10^{-24}} \tag{A1}$$

Assuming hydrostatical equilibrium in the atmosphere, the mass of CO_2 in a column is equal to the pressure between two atmospheric levels divided by the gravitational constant on Mars (374 cm/s^2):

$$n_{CO_2} = \frac{p_{surf} - p_{top}}{374 \times 44 \times 1.66 \times 10^{-24}} = (p_{surf} - p_{top}) \times 3.6595 \times 10^{19} \text{ molecules/cm}^2 \tag{A2}$$

We can obtain the number of H_2O molecules in a similar way:

$$n_{H_2O} = \frac{m_{H_2O}}{18 \times 1.66 \times 10^{-24}} \tag{A3}$$

The water vapor is given in precipitable microns in the TES measurement data, which is the liquid water equivalent in micrometers. The density of liquid water is 1.0 g/cm^3 and a micrometer equals 1×10^{-4} cm, so the number of water molecules is given by:

$$n_{H_2O} = \frac{H_2O_{column} \times 1 \times 10^{-4}}{18 \times 1.66 \times 10^{-24}} = H_2O_{column} \times 3.3456 \times 10^{18} \text{molecules/cm}^2 \tag{A4}$$

To get the water vapor volume mixing ratio, we divide the two values:

$$Q_0 = \frac{n_{H_2O}}{n_{CO_2}} = \frac{H_2O_{column} \times 3.3456 \times 10^{18}}{(p_{surf} - p_{top}) \times 3.6595 \times 10^{22}} = \frac{9.142 \times 10^{-5} \times H_2O_{column}}{p_{surf} - p_{top}} \tag{A5}$$

From here we can calculate RH according to Eqs. (1) and (2).

Appendix B. Methodology

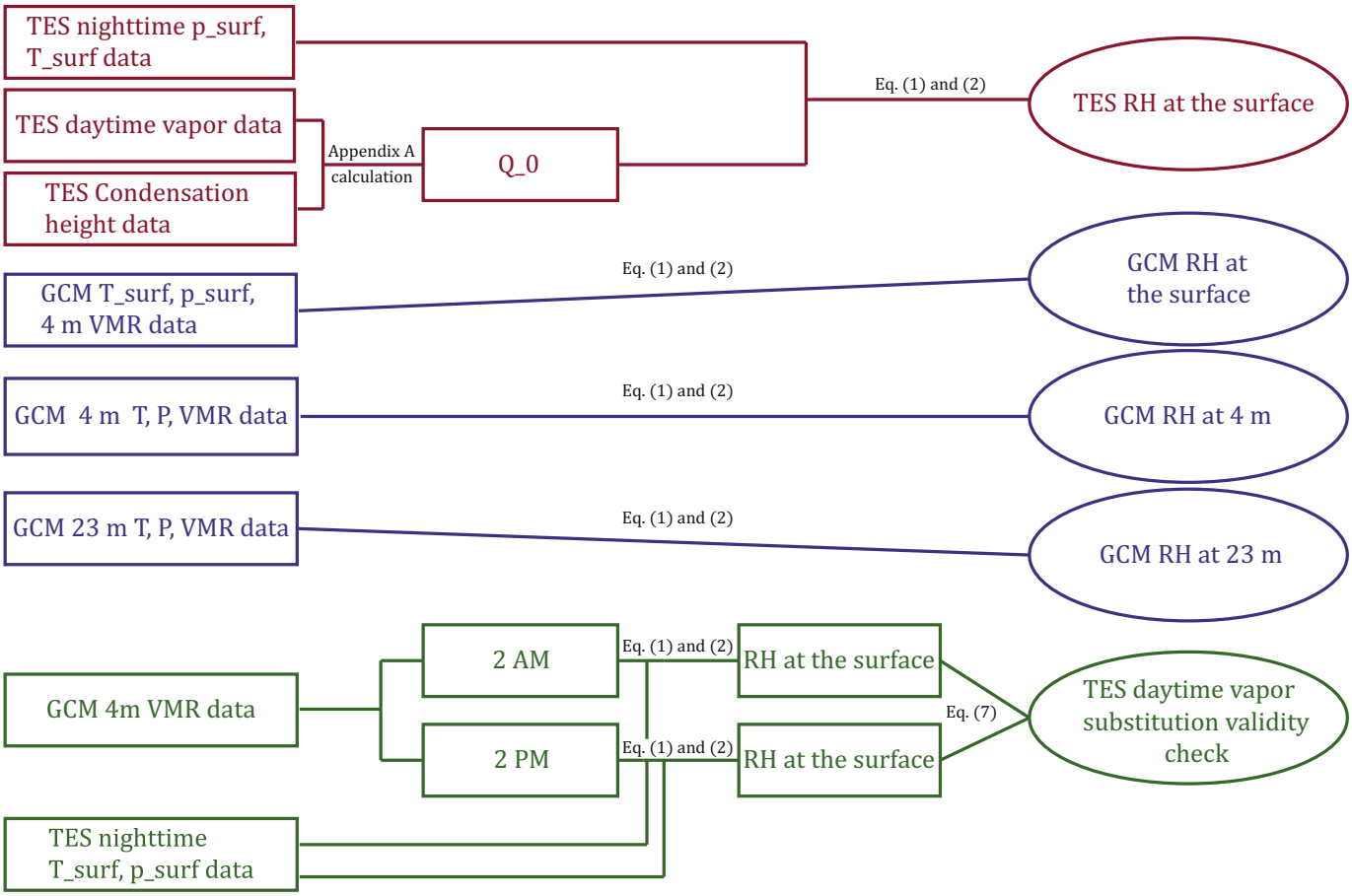

Fig. B.17. Schematic view of our calculations with the input data types shown in the left and output values shown in the right end of the chart.

References

Bapst, J., Bandfield, J.L., Wood, S.E., 2015. Hemispheric asymmetry in Martian seasonal surface water ice from MGS TES. Nov.. Icarus 260, 396–408.

Bass, D.S., Paige, D.A., 2000. Variability of Mars' north polar water ice cap. II. Analysis of Viking IRTM and MAWD Data. Apr.. Icarus 144, 397–409.

Cabrol, N.A., Grin, E.A., 1999. Distribution, classification, and ages of Martian impact crater lakes. Nov.. Icarus 142, 160–172.

Carrozzo, F.G., Bellucci, G., Altieri, F., D'Aversa, E., Bibring, J.-P., 2009. Mapping of water frost and ice at low latitudes on Mars. Oct.. Icarus 203, 406–420.

Clancy, R.T., Grossman, A.W., Wolff, M.J., James, P.B., Rudy, D.J., Billawala, Y.N., Sandor, B.J., Lee, S.W., Muhleman, D.O., 1996. Water Vapor saturation at low altitudes around Mars aphelion: a key to Mars climate? Jul.. Icarus 122, 36–62.

Clancy, R.T., Sandor, B.J., Wolff, M.J., Christensen, P.R., Smith, M.D., Pearl, J.C., Conrath, B.J., Wilson, R.J., 2000. An intercomparison of ground-based millimeter, MGS TES, and Viking atmospheric temperature measurements: seasonal and interannual variability of temperatures and dust loading in the global Mars atmosphere. Apr.. J. Geophys. Res. 105, 9553–9572.

Conrath, B.J., Pearl, J.C., Smith, M.D., Maguire, W.C., Christensen, P.R., Dason, S., Kaelberer, M.S., 2000. Mars global surveyor thermal emission spectrometer (TES) observations: atmospheric temperatures during aerobraking and science phasing. Apr.. J. Geophys. Res. 105, 9509–9520.

Davies, D.W., 1979. The relative humidity of Mars' atmosphere. Dec.. J. Geophys. Res. 84, 8335–8340.

Dundas, C.M., 2018. HiRISE observations of new Martian slope streaks. Mar In: Lunar and Planetary Science Conference, pp. 2026.

Ehlmann, B.L., Swayze, G.A., Milliken, R.E., Mustard, J.F., Clark, R.N., Murchie, S.L., Breit, G.N., Wray, J.J., Gondet, B., Poulet, F., Carter, J., Calvin, W.M., Benzel, W.M., Seelos, K.D., 2016. Discovery of alunite in Cross crater, Terra Sirenum, Mars: evidence for acidic, sulfurous waters. Am. Mineral. 101 (7), 1527. https://doi.org/10.2138/am-2016-5574.

Fassett, C.I., Head, J.W., 2008. Valley network-fed, open-basin lakes on Mars: distribution and implications for Noachian surface and subsurface hydrology. Nov.. Icarus 198, 37–56.

Forget, F., Haberle, R.M., Montmessin, F., Levrard, B., Head, J.W., 2006. Formation of glaciers on Mars by atmospheric precipitation at high obliquity. Jan.. Science 311, 368–371.

Forget, F., Hourdin, F., Fournier, R., Hourdin, C., Talagrand, O., Collins, M., Lewis, S.R., Read, P.L., Huot, J.-P., 1999. Improved general circulation models of the Martian atmosphere from the surface to above 80 km. Oct.. J. Geophys. Res. 104, 24155–24176.

Gargaud, M., Amils, R., Quintanilla, J.C., Cleaves, H.J., Irvine, W.M., Pinti, D.L., Viso, M., 2011. Encyclopedia of Astrobiology.

Gough, R.V., Chevrier, V.F., Tolbert, M.A., 2016. Formation of liquid water at low temperatures via the deliquescence of calcium chloride: implications for Antarctica and Mars. Oct.. Planet. Space Sci. 131, 79–87.

Gurwell, M.A., Bergin, E.A., Melnick, G.J., Ashby, M.L.N., Chin, G., Erickson, N.R., Goldsmith, P.F., Harwit, M., Howe, J.E., Kleiner, S.C., Koch, D.G., Neufeld, D.A., Patten, B.M., Plume, R., Schieder, R., Snell, R.L., Stauffer, J.R., Tolls, V., Wang, Z., Winnewisser, G., Zhang, Y.F., 2000. Submillimeter wave astronomy satellite observations of the Martian atmosphere: temperature and vertical distribution of water vapor. Aug.. Astron. J. Lett. 539, L143–L146.

Haberle, R.M., Jakosky, B.M., 1990. Sublimation and transport of water from the north residual polar CAP on Mars. Feb.. J. Geophys. Res. 95, 1423–1437.

Jakosky, B.M., Carr, M.H., 1985. Possible precipitation of ice at low latitudes of Mars during periods of high obliquity. Jun.. Nature 315, 559–561.

Jakosky, B.M., Farmer, C.B., 1982. The seasonal and global behavior of water vapor in the Mars atmosphere - complete global results of the Viking atmospheric water detector experiment. Apr.. J. Geophys. Res. 87, 2999–3019.

Johnson, J.B., Lorenz, R.D., 2000. Thermophysical properties of Alaskan loess: an analog material for the Martian polar layered terrain? Geophys. Res. Lett. 27 (17), 2769–2772. https://doi.org/10.1029/1999GL011077.

Kate, I.L.t., 2018. Organic molecules on Mars. Science 360 (6393), 1068–1069.

Kereszturi, A., Rivera-Valentin, E.G., 2012. Locations of thin liquid water layers on present-day Mars. Sep.. Icarus 221, 289–295.

Kereszturi, A., Rivera-Valentin, E.G., 2016. Possible water lubricated grain movement in the circumpolar region of Mars. Jun.. Planet. Space Sci. 125, 130–146.

Madeleine, J.-B., Forget, F., Head, J.W., Levrard, B., Montmessin, F., Millour, E., 2009.

Amazonian northern mid-latitude glaciation on Mars: a proposed climate scenario. Oct.. Icarus 203, 390–405.
Maltagliati, L., Montmessin, F., Fedorova, A., Korablev, O., Forget, F., Bertaux, J.-L., 2011a. Evidence of water vapor in excess of saturation in the atmosphere of Mars. Sep.. Science 333, 1868.
Maltagliati, L., Titov, D.V., Encrenaz, T., Melchiorri, R., Forget, F., Keller, H.U., Bibring, J.-P., 2011b. Annual survey of water vapor behavior from the OMEGA mapping spectrometer onboard Mars Express. Jun.. Icarus 213, 480–495.
Martín-Torres, F.J., Zorzano, M.-P., Valentín-Serrano, P., Harri, A.-M., Genzer, M., Kemppinen, O., Rivera-Valentin, E.G., Jun, I., Wray, J., Bo Madsen, M., Goetz, W., McEwen, A.S., Hardgrove, C., Renno, N., Chevrier, V.F., Mischna, M., Navarro-González, R., Martínez-Frías, J., Conrad, P., McConnochie, T., Cockell, C., Berger, G., Vasavada, R.A., Sumner, D., Vaniman, D., 2015. Transient liquid water and water activity at Gale crater on Mars. May. Nat. Geosci. 8, 357–361.
McEwen, A.S., Ojha, L., Dundas, C.M., Mattson, S.S., Byrne, S., Wray, J.J., Cull, S.C., Murchie, S.L., Thomas, N., Gulick, V.C., 2011. Seasonal flows on warm Martian slopes. Aug.. Science 333, 740.
Montmessin, F., Forget, F., Rannou, P., Cabane, M., Haberle, R.M., 2004. Origin and role of water ice clouds in the Martian water cycle as inferred from a general circulation model. Oct.. J. Geophys. Res. Planets 109 (18) E10004.
Moores, J.E., Komguem, L., Whiteway, J.A., Lemmon, M.T., Dickinson, C., Daerden, F., 2011. Observations of near-surface fog at the phoenix Mars landing site. Geophys. Res. Lett. 38 (4). https://doi.org/10.1029/2010GL046315.
Navarro, T., Madeleine, J.-B., Forget, F., Spiga, A., Millour, E., Montmessin, F., Määttänen, A., 2014. Global climate modeling of the Martian water cycle with improved microphysics and radiatively active water ice clouds. Jul.. J. Geophys. Res. Planets 119, 1479–1495.
Nikolakakos, G., Whiteway, J.A., 2018. Laboratory study of adsorption and deliquescence on the surface of Mars. Icarus 308, 221–229 Mars Polar Science V.
Ojha, L., Wilhelm, M.B., Murchie, S.L., McEwen, A.S., Wray, J.J., Hanley, J., Massé, M., Chojnacki, M., 2015. Spectral evidence for hydrated salts in recurring slope lineae on Mars. Nov.. Nat. Geosci. 8, 829–832.
Pál, B., Kereszturi, Á., 2017. Possibility of microscopic liquid water formation at landing sites on Mars and their observational potential. Jan.. Icarus 282, 84–92.
Pankine, A.A., Tamppari, L.K., 2015. Constraints on water vapor vertical distribution at the Phoenix landing site during summer from MGS TES day and night observations. May. Icarus 252, 107–120.
Piqueux, S., Kleinböhl, A., Hayne, P.O., Heavens, N.G., Kass, D.M., McCleese, D.J., Schofield, J.T., Shirley, J.H., 2017. Widespread low-latitude diurnal CO2 frost on Mars. Mar In: Lunar and Planetary Science Conference, pp. 1485.
Pottier, A., Forget, F., Montmessin, F., Navarro, T., Spiga, A., Millour, E., Szantai, A., Madeleine, J.-B., 2017. Unraveling the Martian water cycle with high-resolution global climate simulations. Jul. Icarus 291, 82–106.
Putzig, N.E., Mellon, M.T., Kretke, K.A., Arvidson, R.E., 2005. Global thermal inertia and surface properties of Mars from the MGS mapping mission. Icarus 173 (2), 325–341.
Rennó, N.O., Bos, B.J., Catling, D., Clark, B.C., Drube, L., Fisher, D., Goetz, W., Hviid, S.F., Keller, H.U., Kok, J.F., Kounaves, S.P., Leer, K., Lemmon, M., Madsen, M.B., Markiewicz, W.J., Marshall, J., McKay, C., Mehta, M., Smith, M., Zorzano, M.P., Smith, P.H., Stoker, C., Young, S.M.M., 2009. Possible physical and thermodynamical evidence for liquid water at the Phoenix landing site. Oct.. J. Geophys. Res. Oceans 114 E00E03.
Richardson, M.I., Wilson, R.J., 2002. Investigation of the nature and stability of the Martian seasonal water cycle with a general circulation model. J. Geophys. Res. Planets 107 (E5) 7–1-7–28.
Richardson, M.I., Wilson, R.J., Rodin, A.V., 2002. Water ice clouds in the Martian atmosphere: general circulation model experiments with a simple cloud scheme. Sep.. J. Geophys. Res. Planets 107 5064.
Rivera-Valentín, E.G., Gough, R.V., Chevrier, V.F., Primm, K.M., Martínez, G.M., Tolbert, M., 2018. Constraining the potential liquid water environment at Gale crater, Mars. J. Geophys. Res. Planets 123 (5), 1156–1167. https://doi.org/10.1002/2018JE005558.
Robertson, K., Bish, D., 2011. Stability of phases in the $Mg(ClO_4)_2{\cdot}nH_2O$ system and implications for perchlorate occurrences on Mars. Jul.. J. Geophys. Res. Planets 116 E07006.
Savijärvi, H., 1995. Mars boundary layer modeling: diurnal moisture cycle and soil properties at the Viking Lander 1 Site. Sep.. Icarus 117, 120–127.
Smith, M.D., 2002. The annual cycle of water vapor on Mars as observed by the Thermal Emission Spectrometer. Nov.. J. Geophys. Res. Planets 107 5115.
Smith, M.D., 2004. Interannual variability in TES atmospheric observations of Mars during 1999–2003. Jan.. Icarus 167, 148–165.
Smith, M.D., 2006. TES atmospheric temperature, aerosol optical depth, and water vapor observations 1999–2004. Feb. In: Forget, F., Lopez-Valverde, M.A., Desjean, M.C., Huot, J.P., Lefevre, F., Lebonnois, S. ... Wilson, R.J. (Eds.), Mars Atmosphere Modelling and Observations, pp. 211.
Stamenković, V., Lewis, W., Mischna, M., Fischer, W., 2018. Aerobic Environments on Mars. in review.
Steele, L.J., Lewis, S.R., Patel, M.R., Montmessin, F., Forget, F., Smith, M.D., 2014. The seasonal cycle of water vapour on mars from assimilation of thermal emission spectrometer data. Icarus 237, 97–115.
Tamppari, L.K., Lemmon, M.T., 2016. Vertical water vapor distribution at Phoenix. Sep. In: Sixth International Conference on Mars Polar Science and Exploration. LPI Contributions. 1926. pp. 6027.
Tokano, T., 2003. Spatial inhomogeneity of the Martian subsurface water distribution: implication from a global water cycle model. Jul.. Icarus 164, 50–78.
Tokano, T., 2005. Water on Mars and Life. Springer-Verlag.
Whiteway, J.A., Komguem, L., Dickinson, C., Cook, C., Illnicki, M., Seabrook, J., Popovici, V., Duck, T.J., Davy, R., Taylor, P.A., Pathak, J., Fisher, D., Carswell, A.I., Daly, M., Hipkin, V., Zent, A.P., Hecht, M.H., Wood, S.E., Tamppari, L.K., Renno, N., Moores, J.E., Lemmon, M.T., Daerden, F., Smith, P.H., 2009. Mars water-ice clouds and precipitation. Jul.. Science 325, 68.
Zorzano, M.P., Mateo-Martí, E., Prieto-Ballesteros, O., Osuna, S., Renno, N., 2009. Stability of liquid saline water on present day Mars. Oct.. Geophys. Res. Lett. 36 L20201.